Solvent-Assisted Self-Assembly of Fullerene into Single-Crystal Ultrathin Microribbons as Highly Sensitive UV–Visible Photodetectors

Lang Wei,[†,‡] **Jiannian Yao,**[†,*] **and Hongbing Fu**[†,*]

[†]Beijing National Laboratory for Molecular Sciences (BNLMS), Institute of Chemistry, Chinese Academy of Sciences, Beijing, 100190, People's Republic of China and
[‡]University of Chinese Academy of Sciences, Beijing, 100039, People's Republic of China

ABSTRACT The size, shape, and crystallinity of organic nanostructures play an important role in their physical properties and are mainly determined by the self-assembling kinetics of molecular components often involving the solvent conditions. Here, we reported a kinetically controlled self-assembly of C_{60} assisted by the solvent carbon bisulfide (CS_2) into single-crystal ultrathin microribbons of $2C_{60}\cdot 3CS_2$, upon mixing the poor solvent isopropyl alcohol with a C_{60}/CS_2 stock solution. Surface energy calculations reveal that these microribbons represent a kinetically favored high-energy state as compared with the thermodynamically stable shape of prismatic rods. High-resolution transmission electron microscopy observations clarify that association of CS_2 at the nucleation stage helps to guide and rigidify the formation of $\pi-\pi$ stacking 1D chains of C_{60} through the surrounding CS_2 cage-like structures, which further act as glue, boosting lateral assembly of as-formed 1D chains into untrathin 2D microribbon single crystals. Precise control over the thickness, width, and length of $2C_{60}\cdot 3CS_2$ microribbons was achieved by manipulation of the growth kinetics through adjusting the solvent conditions. Upon heating to 120 °C, sublimation of CS_2 components results in fcc C_{60} microribbons. We found that both microribbons of solvated monoclinic $2C_{60}\cdot 3CS_2$ and pure fcc C_{60} exhibit highly sensitive photoconductivity properties with a spectral response range covering UV to visible. The highest on/off ratio of two-terminal photodetectors based on single ribbons reaches around 250, while the responsivity is about 75.3 A W^{-1} in the UV region and 90.4 A W^{-1} in the visible region.

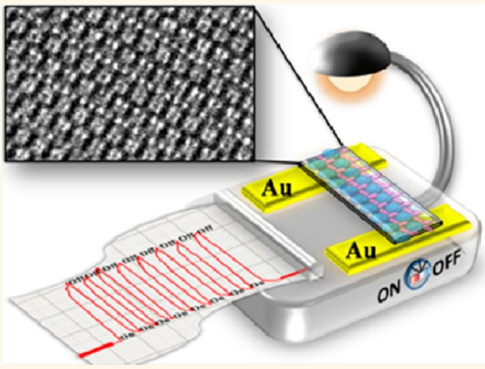

KEYWORDS: fullerene · self-assembly · microribbon · photodetector · nanomaterials

Self-assembled organic nanostructures have been a topic under intense investigation in the past decades,[1−5] because of their potential applications in optoelectronics,[6,7] sensors,[8−10] and biomimics.[11,12] The properties of organic nanostructures depend sensitively not only on their inner molecular organization[13−15] but also on their outer size, morphology, and orientation.[16−21] For instance, close $\pi-\pi$ stacking of conjugated molecules along one-dimensional (1D) nanostructures provides a path for charge transportation, enabling the realization of high-performance field-effect transistors (FETs).[22−24] The optically flat end-faces of well-faceted organic nanowires can function as two reflectors, forming a Fabry–Pérot optical microcavity along the nanowire length.[25−27] Because of a strong optical confinement effect in these structures, active optical waveguides and optically pumped lasers have been successfully demonstrated.[25−27] However, although tailor-made molecules can be obtained by organic synthesis, ensuring that molecules assemble into organic nanostructures with a desirable size, shape, and therefore function remains elusive.[28,29]

In many cases, self-assembly of organic molecules is induced upon mixing a stock solution of molecular building blocks dissolved in a good solvent with a poor solvent (or reversely).[30] Similar to the case of protein fibrillization,[31,32] the solvent conditions play a key role in the formation of self-assembled organic nanostructures.[33−35] On one hand, the solvation effect has a significant impact on the stability of the aggregated structures

* Address correspondence to hongbing.fu@iccas.ac.cn; jnyao@iccas.ac.cn.

Received for review March 30, 2013 and accepted August 12, 2013.

10.1021/nn402889h

that are involved in the nucleation stage of the self-assembling process.[28] On the other hand, the ratio of good/poor solvent influences the nucleation–elongation dynamics, which in turn determine the kinetic pathways toward different complex aggregations.[33−36] It is demonstrated that the internal molecular organization of organic nanostructures might be engineered by focusing on the molecular recognition events between constituent molecular building blocks.[37−40] However, the size and shape of organic nanostructures are mainly controlled by the growth kinetics through which assembly occurs.[18−21,41] Therefore, understanding of the effect of solvents on molecular aggregation kinetics is of utmost importance to control the self-assembling process on the way to obtain well-defined organic nanostructures.

Fullerene (C_{60}) is one of the superstar organic semiconductors, which has been employed in various electronic and photovoltaic devices, such as FETs and bulk heterojunction solar cells.[42−44] The performances of these devices are sensitively related to the size, morphology, and crystalline structures of fullerene and/or its derivatives in the active layer.[45,46] Therefore, for optimizing the device performance great efforts have been dedicated to understanding the mechanism that controls these parameters.[47−49] Here, upon choosing the solvent carbon bisulfide (CS_2), we revealed a kinetically controlled self-assembly of C_{60} into single-crystal ultrathin microribbons of $2C_{60}\cdot 3CS_2$ by mixing the poor solvent isopropyl alcohol (IPA) with a stock solution of C_{60} dissolved in CS_2. Surface energy calculations demonstrate that these microribbons represent a kinetically favored high-energy state as compared with the thermodynamically stable shape of prismatic rods. High-resolution transmission electron microscopy (HRTEM) observations clarify that association of CS_2 at the nucleation stage helps to rigidify and guide the 1D $\pi-\pi$ stacking chains of C_{60} through the formation of CS_2 cage-like structures, which then act as glue, boosting lateral assembly of 1D chains into 2D ribbons. We found that the micoribbon width was defined by the concentration of the C_{60}/CS_2 stock solution, whereas the length and thickness are a function of the added amount of isopropyl alcohol. Upon heating to 120 °C, sublimation of CS_2 components results in fcc C_{60} microribbons. Both microribbons of solvated monoclinic $2C_{60}\cdot 3CS_2$ and pure fcc C_{60} exhibit highly sensitive photoconductivity properties with a spectral response range covering UV to visible. The highest on/off ratio of two-terminal photodetectors based on single ribbons reaches around 250, while the responsitivity is about 75.3 A W^{-1} in the UV region and 90.4 A W^{-1} in the visible region.

RESULTS AND DISCUSSION

Preparation and Characterization of $2C_{60}\cdot 3CS_2$ Microribbons. In our experiment, ultrathin microribbons of C_{60} were prepared by a solution self-assembly method. Typically, a varying volume of IPA (V_{IPA}), which serves as the poor solvent, was dropwisely added into 0.5 mL of a stock solution of C_{60} molecularly dissolved in CS_2 with different concentrations (C_{FULL}). The turbulent mixing of IPA with the C_{60}/CS_2 solution changes the solvent surroundings, thus initiating the nucleating and assembling processes.[18,19] Upon addition of IPA into the C_{60}/CS_2 stock solution, the color of the mixture changed instantly from mauve to turbid yellow. After 30 min, brown-dark precipitates were formed, centrifugally separated from the suspension, and washed using a mixture of IPA/CS_2 (v/v = 1/3) twice prior to vacuum drying.

Scanning electron microscopy (SEM) images in Figure 1A, C, E, and F depict that all samples prepared under different experimental conditions are microribbons, which present a width distributed evenly along the entire length. Transmission electronic microscopy (TEM) images (insets of Figure 1A and C) show that these microribbons are almost transparent under electron beam, indicating that they are ultrathin in nature. Individual microribbons were further imaged by atomic force microscopy (AFM). It can be seen from Figure 1B and D that microribbons have perfectly smooth surfaces and sharp edges. According to the height profiles in the insets of Figure 1B and D, the thickness of corresponding ribbons is also calculated. We found that the length (L), width (W), and thickness (T) of C_{60} microribbons can be readily adjusted by tuning the growth parameters, such as V_{IPA} and/or C_{FULL}.

Table 1 summarizes the sizes of C_{60} microribbons prepared under different preparation conditions. First, we found that the microribbon width is only related to the value of C_{FULL} and decreases with increasing the value of C_{FULL}; for example, W = 5, 4, 3, and 1 μm at C_{FULL} = 0.125 (Figure 1A–D), 0.14 (Figure S1), 0.25 (Figure 1E and F), and 0.32 mg mL^{-1} (Figure S2), respectively. Second, if C_{FULL} is fixed at a certain value that gives a defined ribbon width, the length and thickness of the microribbons could be tuned by adjusting the value of V_{IPA}. Taking C_{FULL} = 0.125 mg mL^{-1} as an example, the width of C_{60} microribbons is constant at W = 5 μm; however, microribbons with L = 30 μm and T = 250 nm were obtained at V_{IPA} = 1.25 mL (Figure 1A and B), and increasing V_{IPA} to 2.0 mL results in shorter and thinner microribbons with L = 20 μm and T = 80 nm (Figure 1C and D). Furthermore, a similar trend was also observed in the cases of C_{FULL} = 0.25 mg/mL and C_{FULL} = 0.32 mg/mL, respectively, at different values of V_{IPA} (Table 1).

Figure 2B displays the selected area electron diffraction (SAED) pattern, recorded by directing the electron beam perpendicular to the top-flat surface of a single ribbon (inset). The monoclinic crystal of $2C_{60}\cdot 3CS_2$ (CCDC No.: 182/1546) belongs to the space group $P2_1/a$, with cell parameters of a = 9.87 Å,

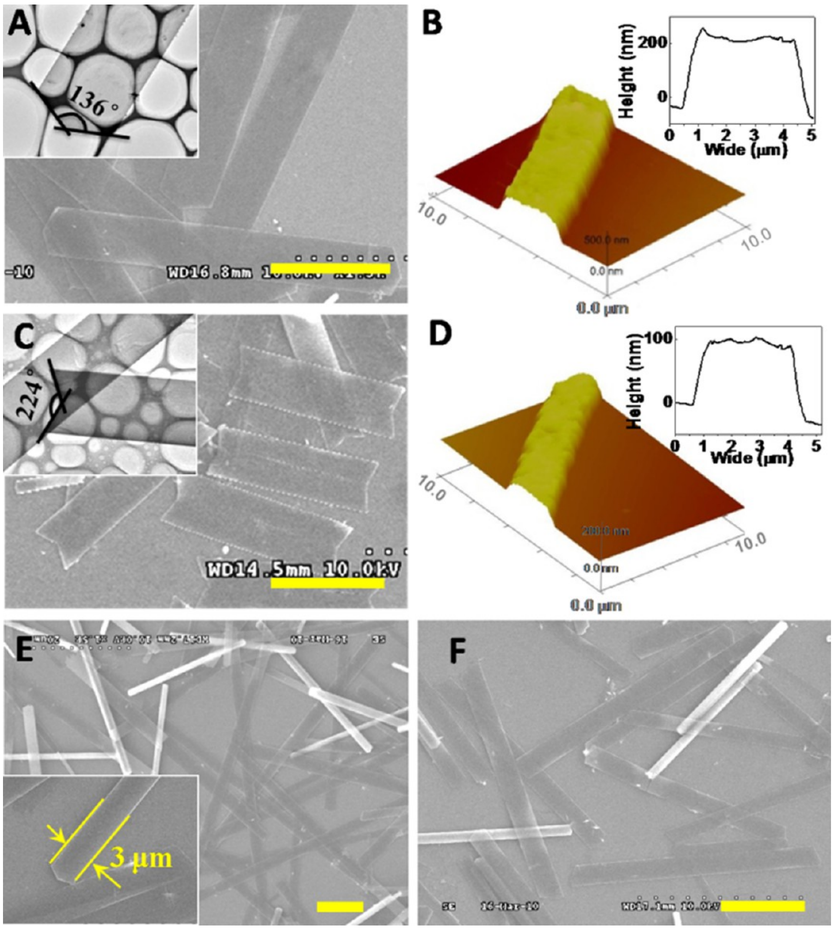

Figure 1. SEM, TEM, and AFM images and corresponding height profiles of microribbons prepared under different conditions: (A and B) C_{FULL} = 0.125 mg/mL, V_{IPA} = 1.25 mL; (C and D) C_{FULL} = 0.125 mg/mL, V_{IPA} = 2.0 mL; (E) C_{FULL} = 0.25 mg/mL, V_{IPA} = 0.70 mL; (F) C_{FULL} = 0.25 mg/mL, V_{IPA} = 0.85 mL. All the scale bars are 10 μm.

TABLE 1. Sizes of C_{60} Microribbons Obtained at Different Preparation Conditions[a]

C_{FULL} (mg mL^{-1})	V_{IPA} (mL)	W (μm)	L (μm)	T (nm)
0.32	0.55	1	100	300
	0.75		50	150
	1.00		15	85
0.25	0.70	3	60	200
	0.85		30	120
	1.50		10	75
0.14	1.5	4	10	100
0.125	1.25	5	30	250
	2.00		20	80

[a] All the sizes reported here have a distribution of <10% by analysis of several tens of microribbons in each case.

b = 25.46 Å, c = 24.67 Å, $\alpha = \gamma$ = 90°, β = 90.05°.[50] Therefore, the square symmetry of the SAED pattern in Figure 2B shows the single-crystal structure of microribbons. The yellow-line-circled set of spots with a short d-spacing value of 4.9 Å is due to (200) Bragg reflection, and the red-line-triangled one with a large d-spacing value of 12.5 Å is due to (002) Bragg reflection. Correlation of Bragg reflections identified in Figure 2B with the orientation of the ribbon shown in the inset makes it clear that the ribbon is preferentially grown along the crystal a-axis with the side surfaces bound by (001) crystal facets and therefore the top/bottom surfaces by (020) facets. This is consistent with X-ray diffraction (XRD) measurements, which measure the crystal planes parallel to the supporting substrate. Indeed, the XRD spectrum of microribbons presents a sequence of peaks corresponding to (020) crystal planes, and other peaks of (hkl) with $h, l \neq 0$, which are observable in the powder pattern, are either weak or not detectable (Figure S3). Combining SAED and XRD results together, we drew a schematic model of microribbons in Figure 2A. Note that the angle between the two terminal side faces of the microribbons is measured to be 136° (insets of Figure 1A and C), in good agreement with the crystallographic data of $\angle(101)/(10\bar{1})$ (Figure 2A).

Figure 2C presents an HRTEM image of a single microribbon of $2C_{60}\cdot 3CS_2$ recorded perpendicular to the top-flat surface, revealing a molecular packing arrangement exactly the same as that within the crystal (020) plane (Figure 2D). It can be seen that C_{60} molecules

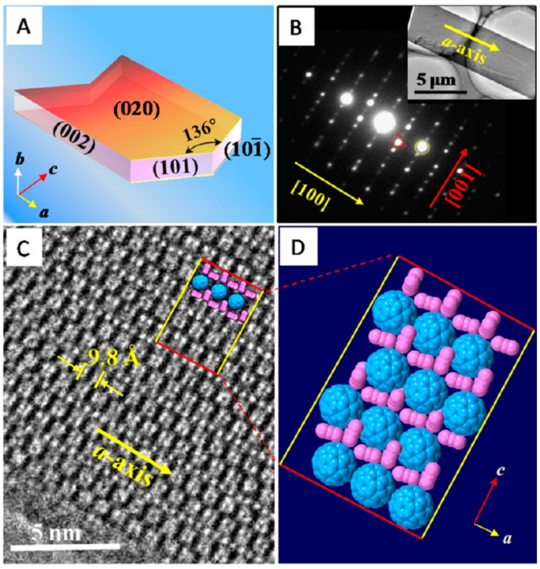

Figure 2. (A) A schematic model for an ultrathin microribbon of $2C_{60}\cdot3CS_2$. (B) SAED pattern and (C) HRTEM image of a single ribbon as shown in the inset of (B). (D) Molecular packing arrangement within the (020) crystal plane.

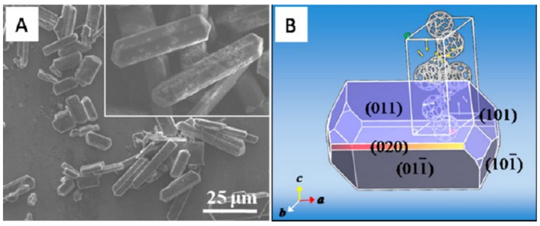

Figure 3. (A) SEM images of prismatic rods obtained after storage of $2C_{60}\cdot3CS_2$ microribbons in a pristine IPA/CS_2 mixture over weeks. (B) Predicted growth morphology for minimum total surface energy calculated by using the Material Studio software package.

TABLE 2. Surface Energies ($\gamma_{(hkl)s}$) of Various Crystal Facets (*hkl*) Calculated by Using the Material Studio Package

(*hkl*)	(011)s	(020)s	(101)s	(002)s	(200)s
$d_{(hkl)s}$ (Å)	17.2	12.37	8.95	11.98	4.82
$\gamma_{(hkl)s}$ (kcal/mol/Å^2)	0.237	0.243	0.255	0.244	0.258

(blue balls) arrange themselves along the crystal *a*-axis, forming a 1D chain-like structure. The intermolecular distance between adjacent C_{60} molecules along the 1D chain is about $d_{(100)} = 9.8$ Å (Figure 2C), which is smaller than the C_{60}–C_{60} distance of 10.23 Å typical in an fcc lattice of pure C_{60} crystal.[51] This suggests that C_{60} molecules along the *a*-axis of a $2C_{60}\cdot3CS_2$ monoclinic crystal (*i.e.*, the microribbon length direction) form a tighter π–π stacking path than that in fcc crystals of pure C_{60}. Most interestingly, we found that the solvent molecules of CS_2 (pink ellipsoids) surround 1D chains of C_{60} (blue balls), producing cage-like structures at the periphery. These CS_2 cages separate 1D chains of C_{60} from each other and stick them together into a 2D layer (Figure 2D).

Predicted Equilibrium Morphology. If as-formed microribbons of $2C_{60}\cdot3CS_2$ were kept in a pristine IPA/CS_2 mixture at ambient conditions over weeks, the morphology of the ribbon would transform to prismatic rods (Figure 3A), probably a result of the Ostwald ripening process.[52] The XRD peaks of the prismatic rods can also be indexed to a monoclinic crystal of $2C_{60}\cdot3CS_2$ (Figure S2B). However, the sequence of peaks corresponding to (020) crystal planes, which are present in the XRD pattern of ultrathin microribbons (Figure S3), could not be observed. Instead, a sequence of peaks corresponding to (011) crystal planes appears (Figure S4B), indicating the abundance of (011) crystal facets on the surfaces of prismatic rods. To gain further insight, we calculated the equilibrium shape of a $2C_{60}\cdot3CS_2$ crystal for minimum total surface energy using the Material Studio software package.[21] It can be seen from Figure 3 that the prismatic rods (Figure 3A) generated by the Ostwald ripening process resemble the calculated equilibrium shape (Figure 3b) in appearance. Although the length direction of prismatic rods is also along the crystal *a*-axis, its surfaces are mainly bound by a (011)s set of facets (Figure 3B). The calculated surface energies ($\gamma_{(hkl)s}$) of crystal faces (*hkl*) follow the order $\gamma_{(011)s} < \gamma_{(020)s} < \gamma_{(101)s}$ (Table 2). Therefore, the total surface energy of $2C_{60}\cdot3CS_2$ microribbons bound mainly by (020)s facets (Figure 2A) should be higher than that of prismatic rods bound mainly by (011)s facets (Figure 3). That is, microribbons of $2C_{60}\cdot3CS_2$ obtained in our experiments have a kinetically stable topology, which can be transformed to thermodynamically stable prismatic rods through the Ostwald ripening process. In this process the high surface energy of microribbons of $2C_{60}\cdot3CS_2$ promotes their redissolution (Figure S2A), whereas material is redeposited on the low-energy surface of prismatic rods.

Kinetical Growth of $2C_{60}\cdot3CS_2$ Microribbons. To further probe the formation process of microribbons, temporal TEM analysis has been performed by capturing the growth morphologies at different growth times in the case of $C_{FULL} = 0.125$ mg/mL and $V_{IPA} = 1.25$ mL (Figure 4A–F). The summarized time-dependent widths and lengths in Figure 4H reveal three distinctive stages: nucleating aggregation (stage I), initial 2D growth (stage II), and preferential 1D growth (stage III). In stage I, the nucleas of $2C_{60}\cdot3CS_2$ formed quickly following the injection of IPA into the C_{60}/CS_2 solution, giving rise to primary plate-like structures with $L \approx 1$ μm and $W \approx 500$ nm (Figure 4A). During stage II about 0.5–2 min after the injection, those initial plate-like structures underwent rapid 2D growth along both the width and the length directions, resulting in microribbons with $W = 2, 3, 5$ μm and $L = 8, 10, 15$ μm for the growth time of 0.5 min (Figure 4B), 1 min (Figure 4C), and 2 min (Figure 4D), respectively. In stage III for

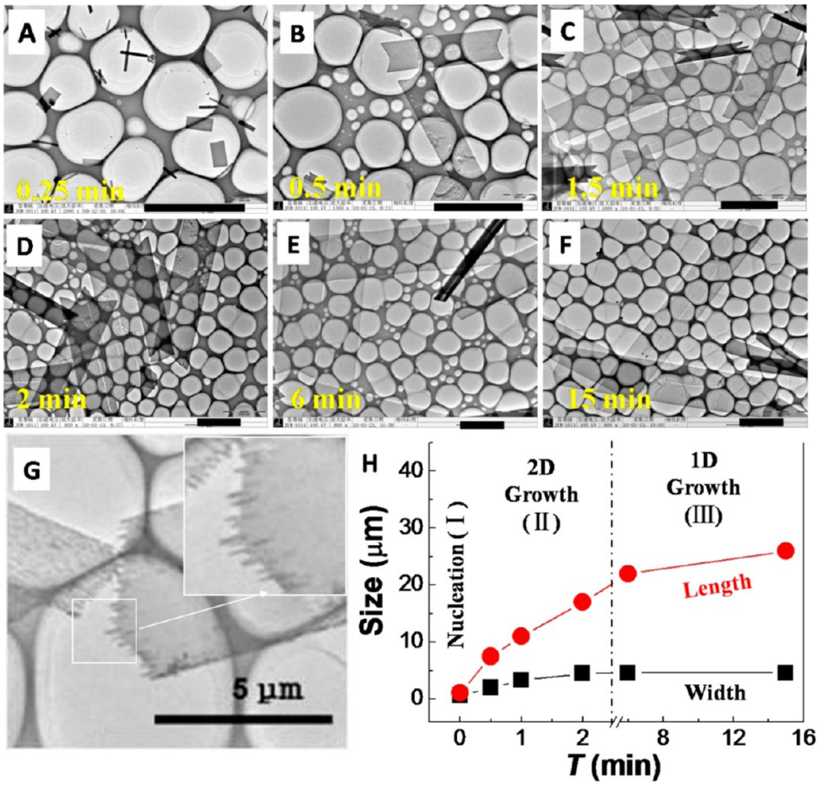

Figure 4. Temporal TEM images of microribbons obtained at different growth times under conditions of C_{FULL} = 0.125 mg/mL and V_{IPA} = 1.25 mL of (A) 0.2, (B) 0.5, (C) 1.0, (D) 2.0, (E) 6.0, and (F) 15.0 min, respectively. (G) Enlarged TEM images showing that whiskers of tens of nanometer in diameter grow out of the microribbon ends. (H) Summarized widths and lengths of microribbons as a function of the growth time. All the scale bars are 5 μm.

growth times longer than 2 min, the width of the ribbons stopped growing and remained almost constant at 5 μm; however, the length of the ribbons kept growing. For instance, microribbons with $L = 20$ μm and $W = 5$ μm were obtained at a growth time of 6 min (Figure 4E). Finally, when the growth time exceeded 15 min, the growth of the microribbon length also terminated, resulting in final products with $L = 30$ μm and $W = 5$ μm (Figure 4F).

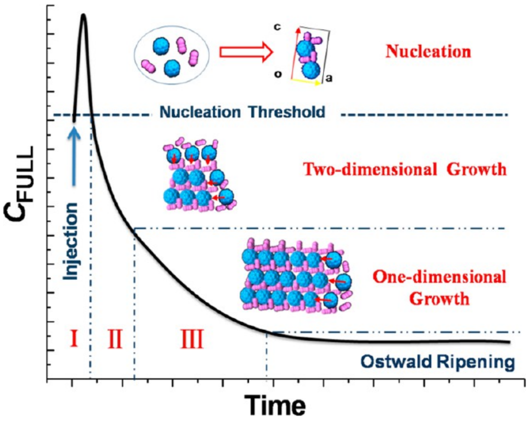

Figure 5. LaMer model for the growth of ultrathin $2C_{60}\cdot 3CS_2$ microribbons.

We further analyzed the roles played by IPA and CS_2 molecules in the growth kinetics of microribbons within the so-called LaMer model (Figure 5).[52,53] In stage I, when the poor solvent IPA is injected into the stock solution of C_{60} dissolved in the good solvent CS_2, a nucleation threshold is immediately achieved due to solvent exchange. Due to the solvation effect, CS_2 molecules participate in the formation of nuclei with C_{60} probably in the form of $2C_{60}\cdot 3CS_2$ (top image in Figure 5). As above-mentioned (Figure 2C), C_{60} molecules prefer to stack along the [100] direction and form tightly packed 1D chains driven by π–π interactions; furthermore, CS_2 forms cage-like structures at the periphery of 1D chains, which not only rigidify these 1D structures but also stick them together to form primary 2D plates. [Sathish and co-workers had reported the formation of 1D nanowhiskers of pure C_{60} from the same set of antisolvent (IPA) and solvent (CS_2) by a liquid–liquid interfacial precipitation (LLIP) method at 5 °C for 24 h.[54] We speculate that the interfacial nucleation induced by antisolvent/solvent diffusion is slow. Therefore, aggregation of C_{60} molecules themselves plays a dominant role in the nucleation stage due to strong π–π interaction, leading to 1D nanowires of pure C_{60} in a triclinic crystal structure by the LLIP method rather than quasi 2D microribbons of $2C_{60}\cdot 3CS_2$ in our experiments.] In stage II, growth along both the [100] (ribbon length) and [001] (ribbon width) directions takes place simultaneously (middle image in Figure 5). Especially, accompanied with the growth of ribbon width along the [001] *c*-axis, there are more association sites available for assembling C_{60} molecules at the ribbon ends (bottom image in Figure 5). Those CS_2 cages at the ribbon ends can serve as templates to guide the 1D growth of C_{60} chain structures. In fact whiskers of tens of nanometers in diameter and hundreds of nanometers in length were often observed to grow out from the ends of ribbons during the 1D growth stage (Figure 4G). Therefore, the rapid 1D growth stage III along the [100] direction leaves $2C_{60}\cdot 3CS_2$ microribbons with top/bottom surfaces bound by high-energy (020)s crystal planes. Our observations abide by the Curtin–Hammett principle: the route to the kinetically favored morphology would be faster.[21,55] As $2C_{60}\cdot 3CS_2$ microribbons are a kinetically achieved product and represent a high-energy state, they can transform to low-energy prismatic rods through the Ostwald ripening process, which are thermodynamically favorable.

Based on the above kinetical model, we can understand the mechanism behind the size control of microribbon width and length. The two key factors exhibited in the growth kinetical model are (i) the duration time of stages I and II and (ii) the number density of nuclei formed in stage I. First, according to Figure 5, the higher the value of C_{FULL}, the faster the aggregation speed. Therefore, the duration time of stages I and II, which determines the microribbon width, is inversely proportional to the value of C_{FULL}; for example, about 3 min for C_{FULL} = 0.125 mg/mL (Figure 4) but 40 s for C_{FULL} = 0.25 mg/mL (Figure S5) lead to the widths of ribbons W = 5 and 3 μm, respectively. Second, at a fixed value of C_{FULL}, the number density of nuclei increases with increasing value of V_{IPA} (stage I). When the total amount of C_{60} growth units is kept constant, the microribbon length becomes shorter with increasing value of V_{IPA} (Table 1) as a result of the increased number density of nuclei (*i.e.*, the number of microribbons).

Transformation into fcc C_{60} Ribbon. According to the TGA spectrum (Figure S6), we found that the microribbons began to lose weight from 50 °C, which is near the boiling point of CS_2. DTA analysis revealed a maximum weight-loss peak at 120 °C with a weight-loss percentage of 10.2%, which is a little bit lower than the theoretical loss of 13.6% of $2C_{60}\cdot 3CS_2$. Figure 6C presents the TEM image of the thermally treated products upon heating $2C_{60}\cdot 3CS_2$ ribbons at 120 °C for 6 h. We found that the original ribbonlike morphology has remained, except that the sizes shrink by 10%. In subsequent XRD analysis of Figure 6B, those signals from monoclinic $2C_{60}\cdot 3CS_2$ crystals gradually disappeared upon heat treatment; meanwhile, the star-marked (111) peak, which matches exactly with fcc C_{60} powder with cell parameters of $a = b = 23.76$ Å and c = 10.08 Å,[51] become dominant in the XRD pattern of treated samples. Moreover, there is no CS_2 molecule observable from the HRTEM image (Figure 6D), in which each C_{60} molecule is closely surrounded by another six C_{60} molecules. Figure 6E shows the SAED pattern of a single ribbon with regular hexagonal diffraction spots, which can be indexed to (101) and $(01\bar{1})$ planes of fcc crystals with similar d-spacing values of 10.23 Å.[51] On the basis of the HRTEM, SAED, and XRD results, we conclude that the up/bottom surfaces of heat-treated fcc-C_{60} ribbons are bound by (111) planes. Remarkably, the volume of an fcc-C_{60} crystal cell is 89.6% of a monoclinic $2C_{60}\cdot 3CS_2$ crystal cell, consistent with the decrease in sizes during microribbon transformation.

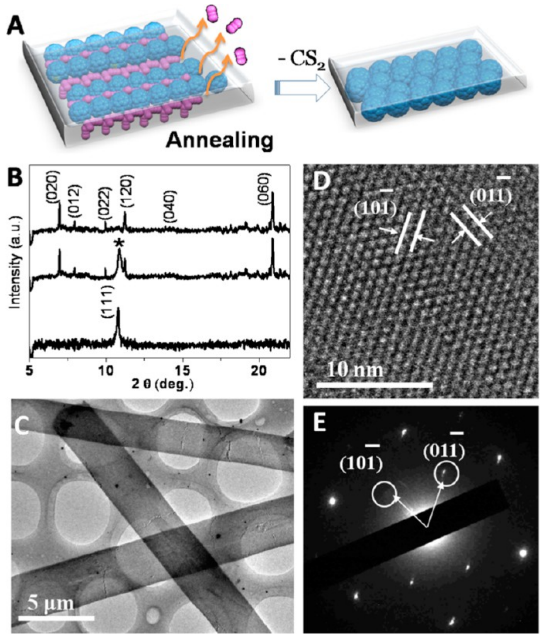

Figure 6. (A) Schematic procedure of removing CS_2 molecules from ultrathin solvated monoclinic $2C_{60}\cdot 3CS_2$ microribbons. (B) Change of XRD patterns from original $2C_{60}\cdot 3CS_2$ ribbons (top line) to heat-annealed fcc C_{60} ribbons (bottom line). (C) TEM image of ultrathin fcc C_{60} ribbons with corresponding (D) HRTEM image and (E) SAED pattern.

Photoresponse. To investigate the photoconductive properties, we carried out two-terminal measurements on single microribbons as presented in Figure 7A. The gap width between the two gold electrodes is around 30 μm (see photograph in Figure S8). Note that the absorption spectra of both $2C_{60}\cdot 3CS_2$ monoclinic and fcc C_{60} microribbons deposited on a quartz plat cover a UV to visible spectral range between 300 and 600 nm (Figure S7), in good agreement with previous reports.[56] In our photoconduction measurement, UV light irradiation was provided by a xenon lamp through a bandpass filter (350–360 nm, Figure S9), and visible light irradiation was generated by an iodine–tungsten lamp (450–750 nm, Figure S10).

As depicted in Figure 7C and D, with UV and/or visible light irradiation on and off, the photocurrent of a solvated monoclinic $2C_{60}\cdot 3CS_2$ microribbon showed two distinct states: a "low" current state in the dark and

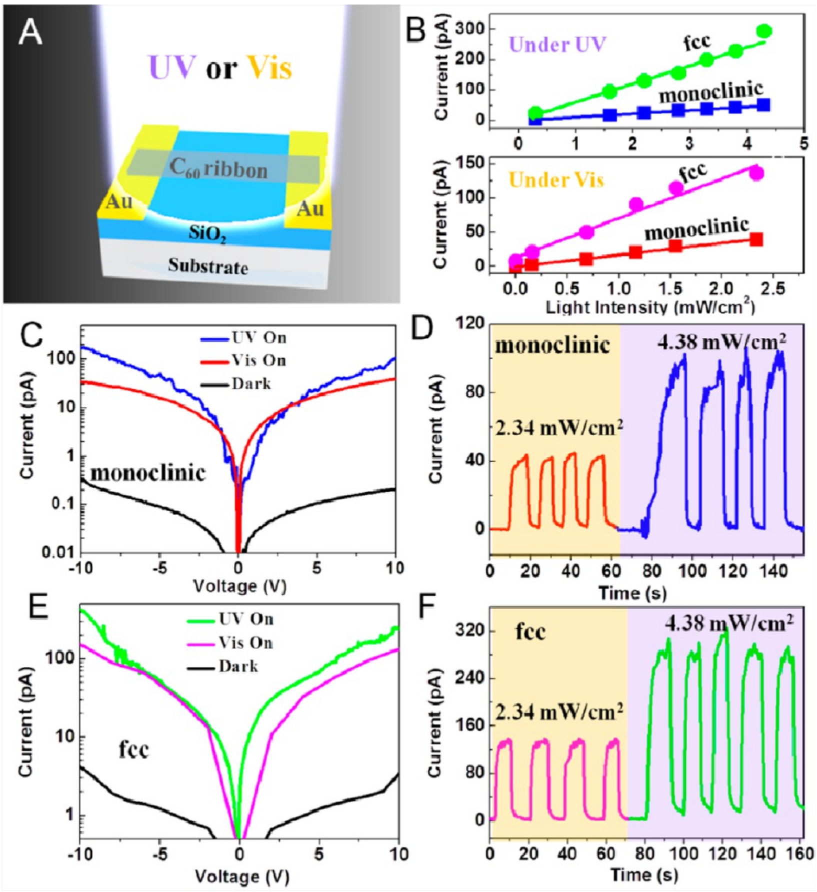

Figure 7. Photoresponse behaviors of ultrathin single-crystalline C_{60} microribbons. (A) Schematic diagram of the two-terminal device. (B) Under UV and visible irradiation, light-dependence of a monoclinic (red and blue lines) and fcc (pink and green lines) C_{60} microribbon at 10 V bias. (C) *I*−*V* characteristics of the monoclinic C_{60} microribbon with and without visible illumination (red line) at a light density of 2.34 mW cm^{-2} and UV illumination (blue line) at a light density of 4.38 mW cm^{-2}. (D) Corresponding time-resolved photoresponse spectrum of a monoclinic C_{60} microribbon. (E) *I*−*V* characteristics of the fcc C_{60} microribbon with and without visible illumination (pink line) at a light density of 2.34 mW cm^{-2} and UV illumination (green line) at a light density of 4.38 mW cm^{-2}. (F) Corresponding time-resolved photoresponse spectrum of an fcc C_{60} microribbon.

a "high" current state under light illumination. In the dark, the current was only 0.2 pA at a bias of 10 V. However, at an incident density of visible light of 2.34 mW cm^{-2}, the photocurrent reaches 40 pA, giving an on/off switching ratio of 200. When the irradiation source was switched to UV light, the photocurrent reached 103 pA with an on/off ratio of 250 at a light density of 4.3 mW cm^{-2}. According to the time-resolved photoresponse spectrum (Figure 7D), the switching between on and off states is fast with similar rising and falling times around 500 ms and could be completed reversibly, allowing the device to act as a high-quality photosensitive switch. As shown in Figure 7B, the photocurrent exhibits a linear response to the light intensity ($I_{ph} \propto$ L.I.). To further evaluate the photoresponse, we calculated two important parameters: the responsivity (R_i), which represents the ratio of the photocurrent to the incident-light power, and the photogain (G), which measures the number of charge carriers passing through the microribbon per absorbed photon.[57,58] The responsivity and the gain are calculated according to eq 1:

TABLE 3. Corresponding On/Off Ratio, Responsivity (R_i), and Photo Gain (G) of Monoclinic and fcc C_{60} Ribbon Devices under Illumination of Visible Light and UV

	visible light (λ = 450−750 nm)			UV (λ = 350−360 nm)		
sample	on/off ratio	R_i (A W^{-1})	G (A W^{-1})	on/off ratio	R_i(A W^{-1})	G (A W^{-1})
monoclinic	200	24	51.36	250	25.2	88.11
fcc	40	75.3	161.14	69	90.4	316.08

$$R_i = \frac{I_{ph}}{\text{L.I.} \times S(1 - T)}, \quad \text{Gain} = R_i(h\nu/q) \qquad (1)$$

in which I_{ph} is the photocurrent, L.I. is the light intensity, S is the exposure area of the microribbon; T is the transmission of light through the microribbon; ν is the frequency of the light, and q is the electron charge.[56] In eq 1, the surface reflection of light is neglected, and the quantum efficiency, defined as the number of photogenerated carriers per photon, is assumed to be unity. It can be seen from Table 3 that the highest R_i of a solvated monoclinic microribbon is 24 A W^{-1} in the visible range and 25.2 A W^{-1} in the UV range under a bias of 10 V. In the visible range, the highest obtained gain for a solvated monoclinic microribbon is 51.36 A W^{-1}, and in the UV range it is 88.11 A W^{-1}. In comparison, inorganic CdS nanowire photodetectors exhibited responsivities and gains of 38 and 100 A W^{-1}, while a photodector based on single-wall carbon nanotubes had a gain of less than 1.[58] These results prove the promising potential of our C_{60} microribbon device as a photoswitch and highly photosensitive detector.

The existence of solvent molecules also plays a key role in the charge dissociation and transportation.[59,60] In Figure 7E, the dark current of an fcc C_{60} microribbon (~3 pA) at 10 V bias was higher than that of a solvated C_{60} microribbon (0.2 pA), which could be attributed to a higher trap density in the fcc-structured microribbon generated during heating transformation. Although the photocurrent of the fcc C_{60} microribbon is also higher than the solvated microribbon, the on/off ratio has dramatically decreased to 40 in the visible range and 69 in the UV range (Figure 7F) due to the higher dark current. However, the fcc C_{60} microribbon exhibited a higher responsitivity and photogain of 75.3 and 161.14 A W^{-1} in the visible range and 90.4 and 316.08 A W^{-1} in the UV range (Table 3).

Finally, it should be noted that both the solvated monoclinic and fcc microribbon devices showed outstanding stability in air. No obvious degradation was observed during hundreds of cycles. The high photoresponse performance together with its high stability demonstrates that ultrathin C_{60} microribbons can serve as excellent microsized optical switches.

CONCLUSIONS

A kinetically controlled self-assembly of C_{60} assisted by the solvent carbon bisulfide into single-crystal ultrathin microribbons of $2C_{60}\cdot 3CS_2$ was successfully demonstrated by mixing the poor solvent isopropyl alcohol with a C_{60}/CS_2 stock solution. Surface energy calculations demonstrated that these microribbons represent a kinetically favored high-energy state as compared with the thermodynamically stable shape of prismatic rods. HRTEM observations elucidate that C_{60} molecules along the crystal [200] direction form the closest $\pi-\pi$ stacking chains, and CS_2 cages at the periphery of the 1D chains not only rigidify these 1D structures but also act as glue to stick them together along the [002] direction into 2D ribbons. Further growth of 2D plates leads to the formation of microribbons with a width controlled by the concentration of the C_{60}/CS_2 stock solution and a length defined by the added amount of IPA. Upon heating to 120 °C, sublimation of CS_2 components results in phase transformation of an fcc C_{60} structure with the microribbon shape remaining. We found that microribbons of both solvated monoclinic $2C_{60}\cdot 3CS_2$ and pure fcc C_{60} exhibit highly sensitive photoconductivity properties with a spectral response range covering the UV to the visible. The highest on/off ratio of two-terminal photodetectors constructed from single ribbons reaches around 250, while the responsitivity is about 75.3 A W^{-1} in the UV region and 90.4 A W^{-1} in the visible region.

METHODS

Materials. Fullerene (C_{60}, 99.5%) was obtained from Aldrich Chemical Co. and used without further purification. Carbon disulfide (CS_2) was purchased from Acros Co. Isopropyl alcohol was provided by Beijing Chemical Agent Ltd. China.

Preparation of Microribbons. Ultrathin microribbons of $2C_{60}\cdot 3CS_2$ were prepared by a solution self-assembly method. Typically, different volumes of IPA (V_{IPA}), which serves as the poor solvent, were dropwisely added into 0.5 mL of a stock solution of C_{60} molecularly dissolved in CS_2 with different concentrations (C_{FULL}). The turbulent mixing of IPA with the C_{60}/CS_2 solution changes the solvent environment, thus initiating the nucleating and assembling processes.[18,19] Upon addition of IPA to the C_{60}/CS_2 stock solution, the color changed instantly from mauve to turbid yellow. After 30 min, dark brown precipitates were formed, centrifugally separated from the suspension, and washed using a mixture of IPA/CS_2 (v/v = 1/3) twice prior to vacuum drying.

Ultrathin microribbons of C_{60} were obtained through the sublimation of $2C_{60}\cdot 3CS_2$ microribbons above 100 °C for 6 h using a tubular furnace.

Morphology and Structure Measurements. The morphologies and sizes of the sample were examined using field emission scanning electron microscopy (FESEM, Hitachi S-4800) at acceleration voltages of 10−15 kV. Prior to analysis, the samples were coated with a thin platinum layer using an Edwards sputter coater. TEM images were collected by a JEOL JEM-2011 transmission electron microscope. One drop of the as-prepared colloidal dispersion was deposited on a carbon-coated copper grid and left to dry under high vacuum, and then observation was performed at room temperature at an accelerating voltage of 200 kV. A Raman scattering spectrum was recorded on a Bruker RFS 100 Raman spectrometer with a 1064.4 nm laser at a power density of 50 mW mm^{-2}. X-ray diffraction patterns were measured by a D/max 2500 X-ray diffractometer with Cu Kα radiation (λ = 1.54050 Å) operated in the 2θ range from 5° to 40°. UV−vis spectra were obtained from a Shimidzu UV-3600. Thermogravimetric analysis was carried out on an SII TG/DTA 6300. The sample was heated from 25 to 800 °C with a heating rate of 10 °C/min. The whole measurement was under nitrogen protection.

Photocurrent Measurements. The microgap electrodes were fabricated by photolithography on a silicon wafer covered with a 300 nm thick SiO_2 dielectric layer. The gold electrode pair is 50 μm long and 30 μm wide, onto which appropriate amounts of nanoribbons were deposited by drop-casting, followed by air-drying in the dark. A tungsten lamp (450−750 nm) was used as the white light source, and a xenon lamp (350−360 nm) was used as the UV light source. The light is guided into the probe station through a glass optical fiber, followed by focusing on the sample through the objective lens. The light power reaching the sample surface was measured by a photon detector. The photocurrent measurements were carried out under air.

Theoretical Calculation. The crystal structure of $2C_{60} \cdot 3CS_2$ was obtained from the Cambridge Structural Database: CCDC No. 182/1546, space group $P2_1/a$, with cell parameters of $a = 9.87$ Å, $b = 25.46$ Å, $c = 24.67$ Å, $\alpha = \gamma = 90°$, $\beta = 90.047(3)°$. The geometric and energy calculations were performed using the Compass and Morphology modules of the Material Studio software.

Conflict of Interest: The authors declare no competing financial interest.

Acknowledgment. This work was supported by the National Natural Science Foundation of China (Nos. 20925309, 21190034, 21221002), the National Basic Research Program of China (973) (2011CB808402, 2013CB933500), and the Chinese Academy of Sciences.

Supporting Information Available: TEM images, XRD pattern, TGA spectrum, and absorption spectrum of ultrathin C_{60} ribbons; additional photograph, $I-V$ spectra, and time-resolved photoresponse spectra of C_{60} ribbons. This information is available free of charge *via* the Internet at http://pubs.acs.org.

REFERENCES AND NOTES

1. Hoeben, F. J. M.; Jonkheijm, P.; Meijer, E. W.; Schenning, A. P. H. J. About Supramolecular Assemblies of π-Conjugated Systems. *Chem. Rev.* **2005**, *105*, 1491–1546.
2. Grimsdale, A. C.; Müllen, K. The Chemistry of Organic Nanomaterials. *Agnew. Chem. Int. Ed.* **2005**, *44*, 5592–5629.
3. Coleman, A. C.; Beierle, J. M.; Stuart, M. C. A.; Maciá, B.; Caroli, G.; Mika, J. T.; van Dijken, D. J.; Chen, J.; Browne, W. R.; Feringa, B. L. Light-Induced Disassembly of Self-Assembled Vesicle-Capped Nanotubes Observed in Real Time. *Nat. Nanotechnol.* **2011**, *6*, 547–552.
4. Rybtchinski, B. Adaptive Supramolecular Nanomaterials Based on Strong Noncovalent Interactions. *ACS Nano* **2011**, *5*, 6791–6818.
5. Aida, T.; Meijer, E. W.; Stupp, S. I. Functional Supramolecular Polymers. *Science* **2012**, *335*, 813–817.
6. Chen, Z.; Lohr, A.; Saha-Möller, C. R.; Würthner, F. Self-Assembled π-Stacks of Functional Dyes in Solution: Structural and Thermodynamic Features. *Chem. Soc. Rev.* **2009**, *38*, 564–584.
7. Zhao, Y.; Fu, H.; Peng, A.; Ma, Y.; Liao, Q.; Yao, J. Construction and Optoelectronic Properties of Organic One-Dimensional Nanostructures. *Acc. Chem. Res.* **2010**, *43*, 409–418.
8. Che, Y.; Yang, X.; Liu, G.; Yu, C.; Ji, H.; Zuo, J.; Zhao, J.; Zang, L. Ultrathin n-Type Organic Nanoribbons with High Photoconductivity and Application in Optoelectronic Vapor Sensing of Explosives. *J. Am. Chem. Soc.* **2010**, *132*, 5743–5750.
9. Niu, Q.; Zhou, Y.; Wang, L.; Peng, J.; Wang, J.; Pei, J.; Cao, Y. Enhancing the Performance of Polymer Light-Emitting Diodes by Integrating Self-Assembled Organic Nanowires. *Adv. Mater.* **2008**, *20*, 964–969.
10. Zang, L.; Che, Y.; Moore, J. S. One-Dimensional Self-Assembly of Planar π-Conjugated Molecules: Adaptable Building Blocks for Organic Nanodevices. *Acc. Chem. Res.* **2008**, *41*, 1596–1608.
11. Palmer, L. C.; Stupp, S. I. Molecular Self-Assembly into One-Dimensional Nanostructures. *Acc. Chem. Res.* **2008**, *41*, 1674–1684.
12. Müller, M. K.; Brunsveld, L. A Supramolecular Polymer as a Self-Assembling Polyvalent Scaffold. *Agnew. Chem., Int. Ed.* **2009**, *48*, 2921–2924.
13. Curtis, M. D.; Cao, J.; Kampf, J. W. Solid-State Packing of Conjugated Oligomers: From π-Stacks to the Herringbone Structure. *J. Am. Chem. Soc.* **2004**, *126*, 4318–4328.
14. Elemans, J. A. A. W.; Van Hameren, R.; Nolte, R. J. M.; Rowan, A. E. Molecular Materials by Self-Assembly of Porphyrins, Phthalocyanines, and Perylenes. *Adv. Mater.* **2006**, *18*, 1251–1266.
15. Würthner, F.; Kaiser, T. E.; Saha-Moller, C. R. J-Aggregates: From Serendipitous Discovery to Supramolecular Engineering of Functional Dye Materials. *Agnew. Chem., Int. Ed.* **2011**, *50*, 3376–3410.
16. Sundar, V. C.; Zaumseil, J.; Podzorov, V.; Menard, E.; Willett, R. L.; Someya, T.; Gershenson, M. E.; Rogers, J. A. Elastomeric Transistor Stamps: Reversible Probing of Charge Transport in Organic Crystals. *Science* **2004**, *303*, 1644–1646.
17. Zhang, X.; Dong, C.; Zapien, J. A.; Ismathullakhan, S.; Kang, Z.; Jie, J.; Zhang, X.; Chang, J. C.; Lee, C.-S.; Lee, S.-T. Polyhedral Organic Microcrystals: From Cubes to Rhombic Dodecahedra. *Agnew. Chem., Int. Ed.* **2009**, *48*, 9121–9123.
18. Huang, L.; Liao, Q.; Shi, Q.; Fu, H.; Ma, J.; Yao, J. Rubrene Micro-crystals from Solution Routes: Their Crystallography, Morphology and Optical Properties. *J. Mater. Chem.* **2010**, *20*, 159–166.
19. Lei, Y.; Liao, Q.; Fu, H.; Yao, J. Phase- and Shape-Controlled Synthesis of Single Crystalline Perylene Nanosheets and Its Optical Properties. *J. Phys. Chem. C* **2009**, *113*, 10038–10043.
20. Kang, L.; Wang, Z.; Cao, Z.; Ma, Y.; Fu, H.; Yao, J. Colloid Chemical Reaction Route to the Preparation of Nearly Monodispersed Perylene Nanoparticles: Size-Tunable Synthesis and Three-Dimensional Self-Organization. *J. Am. Chem. Soc.* **2007**, *129*, 7305–7312.
21. Kang, L.; Fu, H.; Cao, X.; Shi, Q.; Yao, J. Controlled Morphogenesis of Organic Polyhedral Nanocrystals from Cubes, Cubooctahedrons, to Octahedrons by Manipulating the Growth Kinetics. *J. Am. Chem. Soc.* **2011**, *133*, 1895–1901.
22. Li, I. J.; Hu, W. P.; Liu, Y. Q.; Zhu, D. B. Micro- and Nanocrystals of Organic Semiconductors. *Acc. Chem. Res.* **2010**, *43*, 529–540.
23. Liu, S.; Wang, W. M.; Briseno, A. L.; Mannsfeld, S. C. B.; Bao, Z. Controlled Deposition of Crystalline Organic Semiconductors for Field-Effect-Transistor Applications. *Adv. Mater.* **2009**, *21*, 1217–1232.
24. Briseno, A. L.; Mannsfeld, S. C. B.; Reese, C.; Hancock, J. M.; Xiong, Y.; Jenekhe, S. A.; Bao, Z.; Xia, Y. Perylenediimide Nanowires and Their Use in Fabricating Field-Effect Transistors and Complementary Inverters. *Nano Lett.* **2007**, *7*, 2847–2853.
25. Xu, Z.; Liao, Q.; Shi, Q.; Zhang, H.; Yao, J.; Fu, H. Low-Threshold Nanolasers Based on Slab-Nanocrystals of H-Aggregated Organic Semiconductors. *Adv. Mater.* **2012**, *24*, 216–220.
26. Zhao, Y. S.; Peng, A.; Fu, H.; Ma, Y.; Yao, J. Nanowire Waveguides and Ultraviolet Lasers Based on Small Organic Molecules. *Adv. Mater.* **2008**, *20*, 1661–1665.
27. O'Carroll, D.; Lieberwirth, I.; Redmond, G. Microcavity Effects and Optically Pumped Lasing in Single Conjugated Polymer Nanowires. *Nat. Nanotechnol.* **2007**, *2*, 180–184.
28. Jonkheijm, P.; Schoot, P. v. d.; Schenning, A. P. H. J.; Meijer, E. W. Probing the Solvent-Assisted Nucleation Pathway in Chemical Self-Assembly. *Science* **2006**, *313*, 80–83.
29. Wang, Y.; Fu, H.; Peng, A.; Zhao, Y.; Ma, J.; Ma, Y.; Yao, J. Distinct Nanostructures from Isomeric Molecules of Bis(iminopyrrole) Benzenes: Effects of Molecular Structures on Nanostructural Morphologies. *Chem. Commun.* **2007**, *43*, 1623–1625.
30. Palermo, V.; Samori, P. Molecular Self-Assembly across Multiple Length Scales. *Angew. Chem., Int. Ed.* **2007**, *46*, 4428–4432.
31. Knowles, T. P. J.; Buehler, M. J. Nanomechanics of Functional and Pathological Amyloid Materials. *Nat. Naotechnol.* **2011**, *6*, 469–479.
32. England, J. L.; Haran, G. Role of Solvation Effects in Protein Denaturation: From Thermodynamics to Single Molecules and Back. *Annu. Rev. Phys. Chem.* **2011**, *62*, 255–277.
33. Korevaar, P. A.; Schaefer, C.; de Greef, T. F.; Meijer, E. W. Controlling Chemical Self-Assembly by Solvent-Dependent Dynamics. *J. Am. Chem. Soc.* **2012**, *134*, 13482–13491.
34. Kaiser, T. E.; Stepanenko, V.; Wurthner, F. Fluorescent J-Aggregates of Core-Substituted Perylene Bisimides: Studies on Structure-Property Relationship, Nucleation-Elongation Mechanism, and Sergeants-and-Soldiers Principle. *J. Am. Chem. Soc.* **2009**, *131*, 6719–6732.

35. Lei, Y.; Liao, Q.; Fu, H.; Yao, J. Orange-Blue-Orange Triblock One-Dimensional Heterostructures of Organic Microrods for White-Light Emission. *J. Am. Chem. Soc.* **2010**, *132*, 1742–1743.
36. Korevaar, P. A.; George, S. J.; Markvoort, A. J.; Smulders, M. M.; Hilbers, P. A.; Schenning, A. P.; De Greef, T. F.; Meijer, E. W. Pathway Complexity in Supramolecular Polymerization. *Nature* **2012**, *481*, 492–496.
37. Moulton, B.; Zaworotko, M. J. From Molecules to Crystal Engineering: Supramolecular Isomerism and Polymorphism in Network Solids. *Chem. Rev.* **2001**, *101*, 1629–1658.
38. Weissbuch, I.; Addadi, L.; Lahav, M.; Leiserowitz, L. Molecular Recognition at Crystal Interfaces. *Science* **1991**, *253*, 637–645.
39. Zaworotko, M. J. Molecules to Crystals, Crystals to Molecules ... and Back again? *Cryst. Growth Des.* **2007**, *7*, 4–9.
40. Kapadia, P. P.; Ditzler, L. R.; Baltrusaitis, J.; Swenson, D. C.; Tivanski, A. V.; Pigge, F. C. Semiconducting Organic Assemblies Prepared from Tetraphenylethylene Tetracarboxylic Acid and Bis(pyridine)s *via* Charge-Assisted Hydrogen Bonding. *J. Am. Chem. Soc.* **2011**, *133*, 8490–8493.
41. Liu, X. Y.; Boek, E. S.; Briels, W. J.; Bennema, P. Prediction of Crystal Growth Morphology Based on Structural Analysis of the Solid−Fluid Interface. *Nature* **1995**, *374*, 342–345.
42. Itaka, K.; Yamashiro, M.; Yamaguchi, J.; Haemori, M.; Yaginuma, S.; Matsumoto, Y.; Kondo, M.; Koinuma, H. High-Mobility C_{60} Field-Effect Transistors Fabricated on Molecular-Wetting Controlled Substrates. *Adv. Mater.* **2006**, *18*, 1713–1716.
43. Babu, S. S.; Möhwald, H.; Nakanishi, T. Recent Progress in Morphology Control of Supramolecular Fullerene Assemblies and Its Applications. *Chem. Soc. Rev.* **2010**, *39*, 4021–4035.
44. Wei, L.; Wu, Y.; Wang, L.; Fu, H.; Yao, J. Supramolecular Synthesis of Fullerene/Tetracene Hybrid Flowerlike Microstructures of Nanoplates *via* the Charge-Transfer Interactions. *J. Phys. Chem. C* **2011**, *115*, 21629–21634.
45. Li, H.; Tee, B. C.; Cha, J. J.; Cui, Y.; Chung, J. W.; Lee, S. Y.; Bao, Z. High-Mobility Field-Effect Transistors from Large-Area Solution-Grown Aligned C_{60} Single Crystals. *J. Am. Chem. Soc.* **2012**, *134*, 2760–2765.
46. Blom, P. W. M.; Mihailetchi, V. D.; Koster, L. J. A.; Markov, D. E. Device Physics of Polymer:Fullerene Bulk Heterojunction Solar Cells. *Adv. Mater.* **2007**, *19*, 1551–1566.
47. Sathish, M.; Miyazawa, K.; Hill, J. P.; Ariga, K. Solvent Engineering for Shape-Shifter Pure Fullerene (C_{60}). *J. Am. Chem. Soc.* **2009**, *131*, 6372–6373.
48. Wakahara, T.; Sathish, M.; Miyazawa, K. i.; Hu, C.; Tateyama, Y.; Nemoto, Y.; Sasaki, T.; Ito, O. Preparation and Optical Properties of Fullerene/Ferrocene Hybrid Hexagonal Nanosheets and Large-Scale Production of Fullerene Hexagonal Nanosheets. *J. Am. Chem. Soc.* **2009**, *131*, 9940–9944.
49. Park, C.; Song, H. J.; Choi, H. C. The Critical Effect of Solvent Geometry on the Determination of Fullerene (C_{60}) Self-Assembly into Dot, Wire and Disk Structures. *Chem. Commun.* **2009**, *45*, 4803.
50. Olmstead, M. M.; Jiang, F.; Balch, A. L. $2C_{60}\cdot 3CS_2$: Orientational Ordering Accompanies the Reversible Phase Transition at 168 K. *Chem. Commun.* **2000**, *36*, 483–484.
51. Wang, L.; Liu, B.; Liu, D.; Yao, M.; Hou, Y.; Yu, S.; Cui, T.; Li, D.; Zou, G.; Iwasiewicz, A.; Sundqvist, B. Synthesis of Thin, Rectangular C_{60} Nanorods Using m-Xylene as a Shape Controller. *Adv. Mater.* **2006**, *18*, 1883–1888.
52. Murray, C. B.; Kagan, C. R. Synthesis and Characterization of Monodisperse Nanocrystals and Close-Packed Nanocrystal Assemblies. *Annu. Rev. Mater. Sci.* **2000**, *30*, 545–610.
53. Lamer, V. K.; Dinegar, R. H. Theory, Production and Mechanism of Formation of Monodispersed Hydrosols. *J. Am. Chem. Soc.* **1950**, *72*, 4847–4854.
54. Sathish, M.; Miyazawa, K. Synthesis and Characterization of Fullerene Nanowhiskers by Liquid-Liquid Interfacial Precipitation: Influence of C_{60} Solubility. *Molecules* **2012**, *17*, 3858–3865.
55. Desiraju, G. R. Cryptic Crystallography. *Nat. Mater.* **2002**, *1*, 77–79.
56. Guldi, D. M. Excited-State Properties of C_{60} Fullerene Derivatives. *Acc. Chem. Res.* **2000**, *33*, 695–703.
57. Zhou, Y.; Wang, L.; Wang, J.; Pei, J.; Cao, Y. Highly Sensitive, Air-Stable Photodetectors Based on Single Organic Sub-Micrometer Ribbons Self-Assembled through Solution Processing. *Adv. Mater.* **2008**, *20*, 3745–3749.
58. Talapin, D. V.; Lee, J. S.; Kovalenko, M. V.; Shevchenko, E. V. Prospects of Colloidal Nanocrystals for Electronic and Optoelectronic Applications. *Chem. Rev.* **2010**, *110*, 389–458.
59. Yang, J.; Lim, H.; Choi, H. C.; Shin, H. S. Wavelength-Selective Silencing of Photocurrent in Au-Coated C_{60} Wire Hybrid. *Chem. Commun.* **2010**, *46*, 2575–2577.
60. Ogawa, K.; Kato, T.; Ikegami, A.; Tsuji, H.; Aoki, N.; Ochiai, Y.; Bird, J. P. Electrical Properties of Field-Effect Transistors Based on C_{60} Nanowhiskers. *Appl. Phys. Lett.* **2006**, *88*, 112109.